



# Effect of initial microstructure on the hot compression deformation behavior of a 2219 aluminum alloy

Jing Zhang<sup>\*</sup>, Boquan Chen, Baoxiang Zhang

College of Materials Science and Engineering, Chongqing University, Chongqing 400044, China

## ARTICLE INFO

### Article history:

Received 8 May 2011

Accepted 26 July 2011

Available online 3 August 2011

### Keywords:

A. Non-ferrous metals and alloys

C. Forming

F. Microstructure

## ABSTRACT

This paper examines the effect of initial microstructure on the deformation behavior of a 2219 aluminum alloy. Based on the manufacturing practice of the alloy, three different initial microstructures were designed, the newly as-homogenized microstructure (state 3), the as-solutionized microstructure (state 2) and the as-aged microstructure (state 1). Hot compression tests in the temperature range of 350–450 °C and strain rate 0.01–10 s<sup>−1</sup> were conducted to evaluate their hot-working characteristics. Constitutive constants for each initial state were obtained and compared. The results showed that state 2 always showed the highest deformation resistance and state 1 the lowest under the same deformation conditions. Furthermore, state 2 was the most sensitive to the change of the deformation conditions, while state 1 the least. The activation energies for deformation  $Q$  for state 1, state 2 and state 3 were computed to be 166, 223 and 172 kJ mol<sup>−1</sup>, respectively. At a lower strain rate of 0.01 s<sup>−1</sup> only dynamic recovery occurred. The dynamic recrystallization degree increased with the increase of the strain rate. Moreover, it was found that the minimum strain rate which could stimulate recrystallization shifted to lower value for state 2 compared with state 3. When deformed at a high strain rate of 10 s<sup>−1</sup>, the alloy exhibited unstable flow deformation; in addition, state 1 always manifested uneven grain structures after deformation under the experimental conditions. The influencing mechanism of the microstructural characteristics on the deformation behaviors is discussed.

© 2011 Elsevier Ltd. All rights reserved.

## 1. Introduction

Al–Cu alloys are widely used in various structural components of transportation and aircraft industry for their excellent combined properties, such as high strength and toughness and sound weldability [1–3]. These products are generally hot worked by extrusion, rolling or forging, from a cast billet. Hence, the hot-working characteristics of billet are crucial to forming process; which are in turn dictated by its microstructure, in addition to the hot deformation regimes. Furthermore, Al–Cu alloys are aging-sensitive [1,2,4,5], which implies that cooling manner from an isothermal holding, or even the duration in between the hot-working processes, will affect alloy microstructure and subsequent deformation behaviors [6,7]. However, existing reports [1,4,8,9] concern about the interaction between creep deformation and Cu, where Cu is either in the form of solute atoms in the high temperature range from 500 to 580 °C, or precipitates in the low temperature range from 100 to 250 °C, at initial strain rates of less than 10<sup>−2</sup> s<sup>−1</sup>. There are only limited reports on the deformation behaviors in the intermediate temperature range from 250 to 500 °C,

which is widely used in practical hot processing of Al–Cu alloys [8]. Moreover, little research has been carried out about the influence of different microstructures on the deformation behaviors of the alloys.

This paper examines the effects of different microstructures on the deformation behaviors of a 2219 Al alloy. The cast billet was undergone three typical heat treatments, according to the manufacturing practice, in order to obtain different initial microstructures. Hot compression tests in the temperature range of 350–450 °C and strain rate 0.01–10 s<sup>−1</sup> were then used to evaluate their hot-working characteristics. Constitutive constants for each initial state were obtained and compared. The aim of the present study is to optimize the processing conditions and provide basic data for computational modeling to improve the forming performance and properties of the alloy.

## 2. Experimental procedures

The 2219 aluminum alloy with the chemical composition Al–6.4%Cu–0.3%Mn–0.1%V–0.17%Zr–0.06%Ti–0.15%Fe–0.05%Si was prepared by direct chill casting. The as-cast billet was then undergone three different heat treatments to change the initial microstructure. Determination of these heat treatment conditions was

<sup>\*</sup> Corresponding author. Tel.: +86 23 65111167; fax: +86 23 65102635.

E-mail address: [jingzhang@cqu.edu.cn](mailto:jingzhang@cqu.edu.cn) (J. Zhang).

based on the possible manufacturing practice of the alloy. One was homogenized at 535 °C for 10 h and cooled slowly in a furnace, followed by natural aging in open air (designated as state 1). After that, some of the billets was reheated at 460 °C for 10 h then quenched in water of around 50 °C to provide a super solid solution structure of the alloy (designated as state 2); while the other was reheated to 535 °C for 0.5 h and cooled slowly in a furnace to provide a newly as-homogenized structure (designated as state 3).

Cylindrical specimens 10 mm in diameter and 12 mm in length were machined from each heat-treated alloy billet for hot compression tests, using a Gleeble 1500D thermo-mechanical simulator. Temperature was varied from 350 to 450 °C in increments of 50 °C. At every temperature, tests were performed at strain rates of 0.01, 0.1, 3 and 10 s<sup>-1</sup>, respectively, to a true strain of one. Before hot uniaxial compression, the specimen was heated at a rate of 10 °C/s and soaked for 60 s at the preset temperature to ensure a homogenous temperature distribution throughout the specimen. A thermocouple was spot-welded onto the surface of the specimen in order to measure and control the actual specimen temperature. To minimize the friction between the specimen and anvil during hot deformation, graphite foils were used as lubricant. After the deformation, specimens were quenched immediately in 50 °C-water to preserve the as-deformed microstructures.

The microstructures of specimens were examined by optical microscopy under both normal light and polarized light. For optical observation, specimens were grounded according to standard methods and then electropolished (20% HClO<sub>4</sub> + 80% ethanol) and anodized (43% H<sub>3</sub>PO<sub>4</sub> + 38% H<sub>2</sub>SO<sub>4</sub> + 19% H<sub>2</sub>O). The average grain size and volume fraction of the compounds were measured using the Transcend Tciimage image-analysis software. Phase constitutions for each heat-treated alloy were determined by a Rigaku D/max 2500PC X-ray diffractometer with the use of Cu K $\alpha$  radiation.

### 3. Results and discussion

#### 3.1. Initial microstructures

The optical microstructures of the three heat-treated alloys are shown in Fig. 1. It can be seen that there are still some undissolved primary eutectic compounds distributed along grain boundaries,

especially at triple grain boundaries. Beside these coarse intermetallics, large quantities of small particles are clearly observed, which were most probably formed by precipitation from the  $\alpha$ -Al matrix during the cooling process following an isothermal holding. The total volume fraction of the second phase were measured to be almost the same for states 2 and 3, being about 21%; whilst for state 1 the value was 26%, a bit higher than the former two. This is largely attributed to the longer holding time at high temperatures which promoted the dissolution of primary eutectic compounds for states 2 and 3. In addition, the volume fraction of the small particles in state 1 was the highest among the three alloys. This is certain since the alloy was undergone natural aging. Detailed comparison between states 2 and 3 revealed that state 2 had more large compounds (13%) but less small particles (8%) than state 3 (9% and 12%, respectively), indicating a coalescence and growth of the undissolved particles during the 460 °C isothermal holding and an inhibition of precipitation from the matrix during the quenching in state 2.

The phase constitutions were revealed by XRD, as shown in Fig. 2. The second phases were Al<sub>2</sub>Cu and Al<sub>7</sub>Cu<sub>2</sub>Fe in common but with different intensities, indicating the percentage of these phases varied from one alloy with another. The remarkable difference among the three states lies in the Al–Fe–Si phase. While there is a fairly strong peak for state 1, the peak intensity decreases sharply for state 3, and even no diffraction peak could be detected at all for state 2. Al–Fe–Si phase is always present in Al alloys containing Fe and Si as impurity elements [10,11]. The stoichiometric ratio of the elements in the phase may vary in a broad range depending upon alloy composition, casting and cooling speed, and heat treatment conditions as well [12–17]. Precipitation of the phase will consume solute Si thus decreasing the concentration of Si in the matrix. Therefore, it is conceivable that the concentration of Si in the  $\alpha$ -Al solid solution was the highest for state 2.

#### 3.2. Flow stress–strain curves during hot compression tests

Selected true stress–true strain curves ( $\sigma$ – $\epsilon$  curves) obtained during the hot compression tests are presented in Fig. 3. The flow stress decreases as the temperature increases or the strain rate

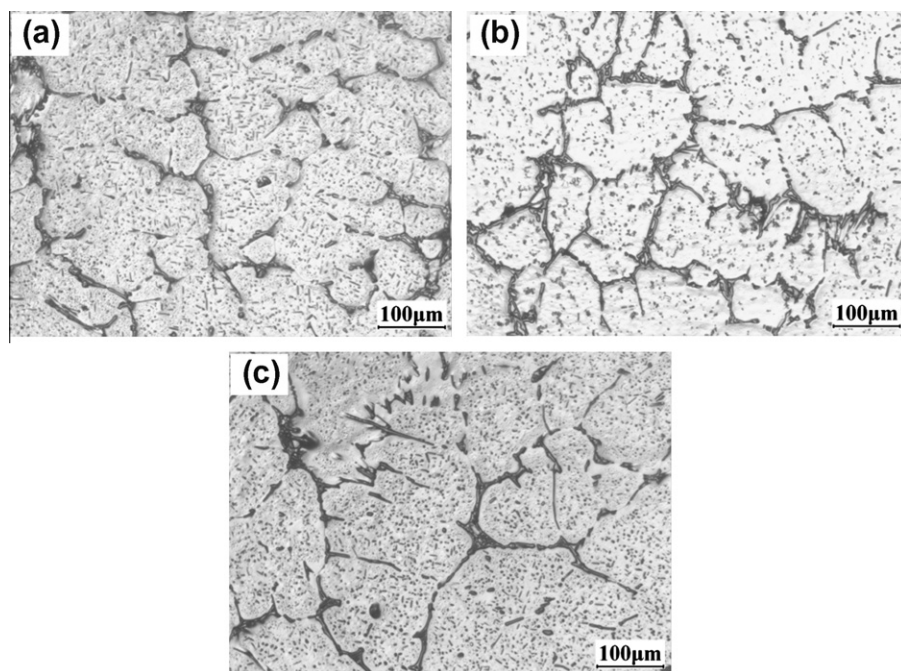


Fig. 1. Optical micrographs of the three heat-treated alloys: (a) state 1; (b) state 2; (c) state 3.

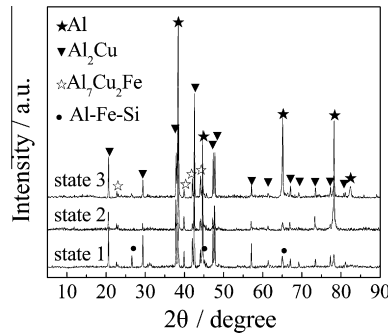


Fig. 2. XRD patterns of the three heat-treated alloys.

decreases. The peak flow stress is generally followed by a steady state region or a slight decrease of the flow stress with strain, implying the work softening, probably due to dynamic recovery and dynamic recrystallization, prevails over the work hardening with strain during deformation.

The influence of different initial microstructures on the flow curves can be clearly seen in Fig. 4. Comparison between these curves revealed the following three characteristics. Firstly, the flow stresses are markedly different for different initial states under the same deformation conditions. The flow stresses for state 2 are always the highest and those for state 1 the lowest. This is largely to be the result of the highest concentration of Si in the  $\alpha$ -Al matrix for state 2. It has been known that dissolved Si and Fe dramatically increase the work-hardening rate of Al [18–20], resulting in a higher deformation resistance. Precipitation of Al–Fe–Si phase will decrease the concentration of Si in the matrix, leading to a decreased deformation resistance. XRD analysis results showed the most amount of the Al–Fe–Si phase in state 1, which was well consistent with the lowest flow stresses among the three initial states. Moreover, this difference is especially obvious when deformed at lower temperatures and higher strain rates, where the Zener–Hollomon parameter,  $Z = \dot{\epsilon} \exp[Q/RT]$ , which describes the combined effects

of the deformation temperature  $T$  and strain rate [21], holds relatively high values. Generally, with increasing  $Z$ , dynamic recovery  $\dot{\epsilon}$  and dynamic recrystallization become less active, and greater hardening occurs during deformation. This feature suggests that the dissolved Si further strengthened the hardening process during the deformation.

The second observation is that at high strain rates of  $3 \text{ s}^{-1}$  and  $10 \text{ s}^{-1}$ , especially  $10 \text{ s}^{-1}$ , the flow curves wave obviously, as shown in Fig. 4c–d. This plastic instability is considered to be the Portevin–Le Chatelier (PLC) effect due to dynamic strain aging (DSA), i.e. dynamic interaction between mobile dislocations and diffusing solute atoms. In addition, it is interesting to note that while state 3 still underwent a continuous deformation in the whole strain range, states 1 and 2 both showed an abrupt decline of flow stresses when strained to approximately 0.6 during the deformation. Combined with the microstructural analysis, this is likely attributed to the relatively higher solid solution degree in state 2 and larger volume fraction of small precipitates formed during natural aging in state 1, which made precipitation or dissolution possibly occurring during the deformation. The microstructural change was certain to result in a change of the deformation behavior. However, detailed mechanism needs further studying. In industrial practice, such a wave or abrupt decline always indicates an unstable flow deformation, which should be avoided. From this point of view, the deformation strain rate of the alloy should not exceed  $\sim 10 \text{ s}^{-1}$ . Under the circumstances where a large strain rate is inevitably avoided, microstructure of state 3 is comparatively favorable.

The third clear difference in flow curves among the three heat-treated alloys is their different sensitivity to the change of the deformation conditions. Under various deformation conditions other than strain rate of  $10 \text{ s}^{-1}$  to ensure a stable deformation, the variation intervals of the peak flow stresses are from 32 to 99 MPa, from 35 to 132 MPa and from 33 to 118 MPa for states 1–3, respectively. The wider the interval is, the more sensitivity of the alloy to the deformation conditions. These figures therefore indicate that state 1 is the least sensitive, while state 2 is the most. The low sensitivity normally implies an easy control and a stable

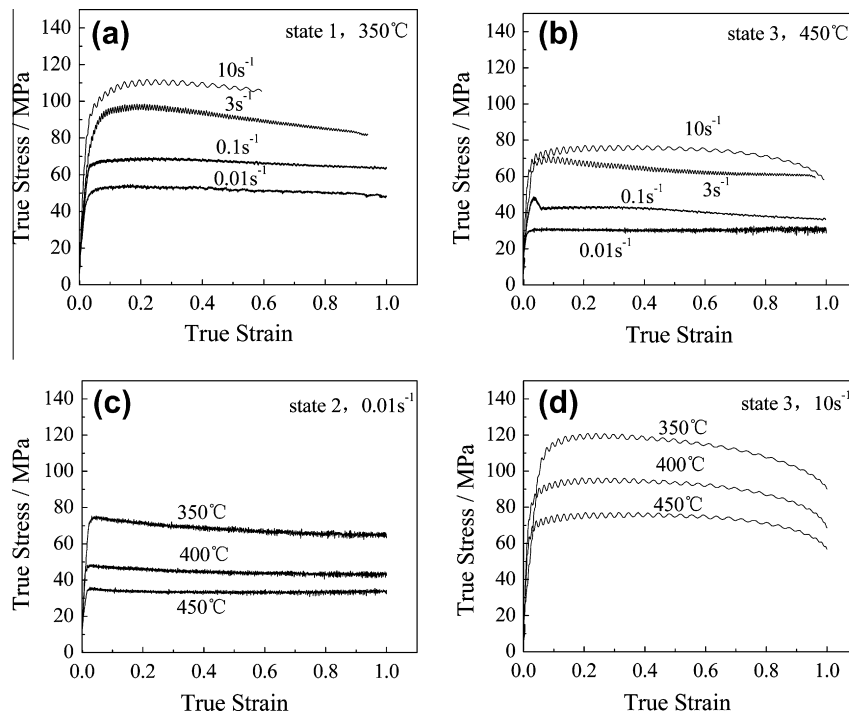
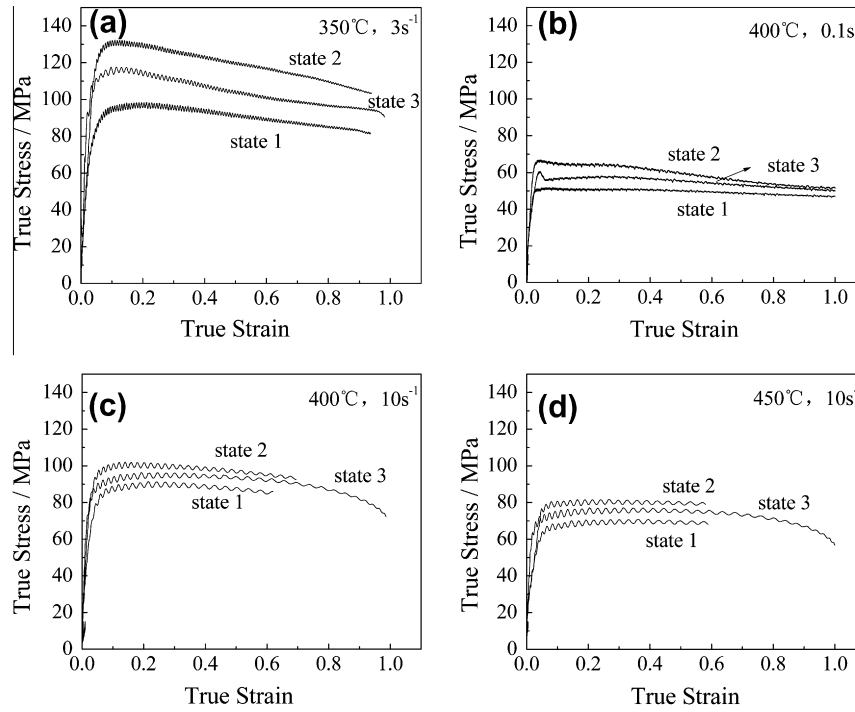
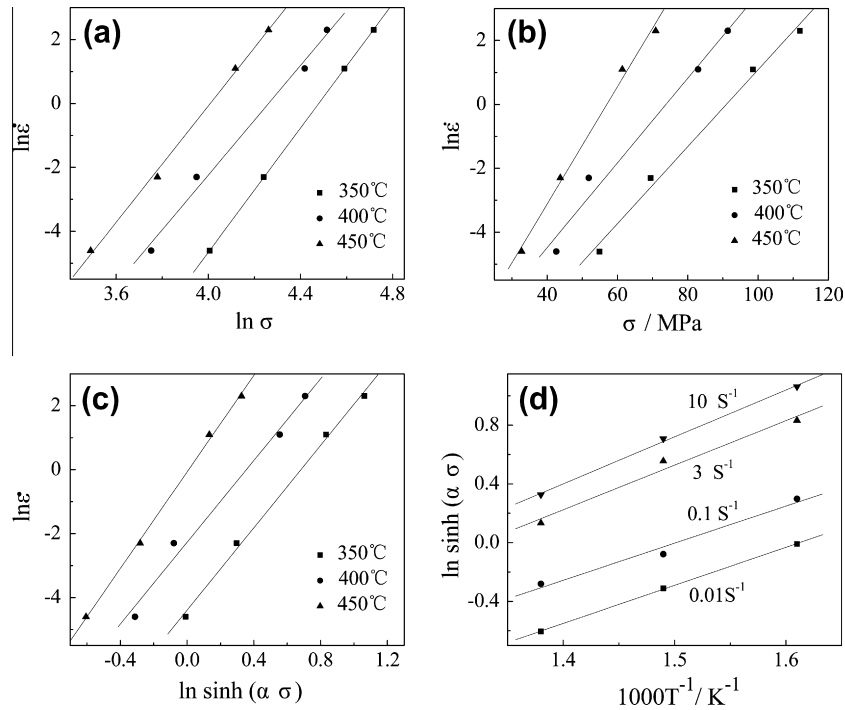


Fig. 3. True stress–true strain curves for different initial states under selected deformation conditions: (a) state 1,  $350 \text{ }^{\circ}\text{C}$ ; (b) state 3,  $450 \text{ }^{\circ}\text{C}$ ; (c) state 2,  $0.01 \text{ s}^{-1}$ ; (d) state 3,  $10 \text{ s}^{-1}$ .



**Fig. 4.** The influence of different initial microstructures on the flow curves deformed at selected conditions: (a) 350 °C and a strain rate of 3 s<sup>-1</sup>; (b) 400 °C and a strain rate of 0.1 s<sup>-1</sup>; (c) 400 °C and a strain rate of 10 s<sup>-1</sup>; (d) 450 °C and a strain rate of 10 s<sup>-1</sup>.



**Fig. 5.** Relationship between (a)  $\ln(\sigma)$  and  $\ln(\dot{\epsilon})$ ; (b)  $\sigma$  and  $\ln(\dot{\epsilon})$ ; (c)  $\ln(\dot{\epsilon})$  and  $\ln[\sinh(\alpha\sigma)]$ ; (d)  $\ln[\sinh(\alpha\sigma)]$  and  $1000/T$  for state 1.

performance in manufacturing processes, which is highly appreciated. From this point of view, state 1 is preferred whilst state 2 should be avoided.

### 3.3. Constitutive equations

Constitutive equation is commonly used to calculate the flow stress of a material during deformation. It is generally accepted that the following sine hyperbolic equation, which combines the power law and the exponential law in, respectively, low and high

stress ranges, is suitable for constitutive analysis over wide ranges of deformation temperatures and strain rates [2,22–24]:

$$Z = \dot{\epsilon} \exp(Q/RT) = A[\sinh(\alpha\sigma)]^n \quad (1)$$

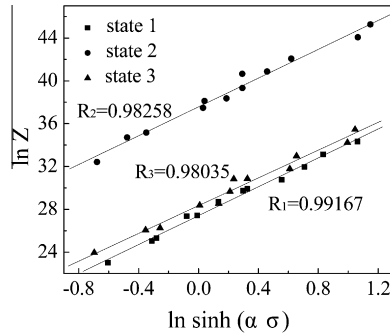
where  $A$  is a constant,  $\alpha$  is a temperature-independent material constant,  $n$  is the stress exponent,  $R$  is the universal gas constant, and  $Q$  the activation energy for deformation.  $\sigma$  can be either peak stress or steady flow stress. In this paper, peak flow stress was taken into the calculation.



**Table 1**

Constitutive constants in Eq. (1) for the three heat-treated alloys.

Alloys	$\alpha/\text{MPa}^{-1}$	$Q/(\text{kJ mol}^{-1})$	$n$	$\ln A/\ln \text{s}^{-1}$
State 1	0.01594	165.9	6.7461	27.41
State 2	0.01351	222.5	6.7233	37.57
State 3	0.01464	171.7	6.4817	28.34

**Fig. 6.** Relationship between  $\ln[\sinh h(\alpha\sigma)]$  and  $\ln(Z)$  under different deformation conditions.

The logarithm was taken and Eq. (1) was rearranged:

$$\ln(\dot{\epsilon}) = \ln A + n \ln[\sinh h(\alpha\sigma)] - Q/RT \quad (2)$$

An approximate value of  $\alpha$  was calculated by  $a = \frac{\beta}{n} \approx \frac{\beta}{n_1}$ , where  $n_1$  and  $\beta$  are the average slopes of  $\ln(\sigma) - \ln(\dot{\epsilon})$  and  $\sigma - \ln(\dot{\epsilon})$  lines at constant  $T$ , respectively [2,22,23]. As an example, the plots of  $\ln(\sigma) - \ln(\dot{\epsilon})$  and  $\sigma - \ln(\dot{\epsilon})$  at constant  $T$  for state 1 are given in Fig. 5a and b. The slope of the  $\ln[\sinh h(\alpha\sigma)]$  against  $\ln \dot{\epsilon}$  plot then gave the value of  $1/n$  (Fig. 5c).

Rearranging Eq. (2) and differentiating with respect to  $1/T$  gave an expression for the activation energy  $Q$ :

$$Q = R \left[ \frac{\partial \ln \dot{\epsilon}}{\partial \ln[\sinh h(\alpha\sigma)]} \right]_T \left[ \frac{\partial \ln[\sinh h(\alpha\sigma)]}{\partial (1/T)} \right]_{\dot{\epsilon}} = RnS \quad (3)$$

where  $S$  is the average slope of the lines in the  $\ln[\sinh h(\alpha\sigma)]$  against  $1000/T$  plots, as seen in Fig. 5d for state 1.

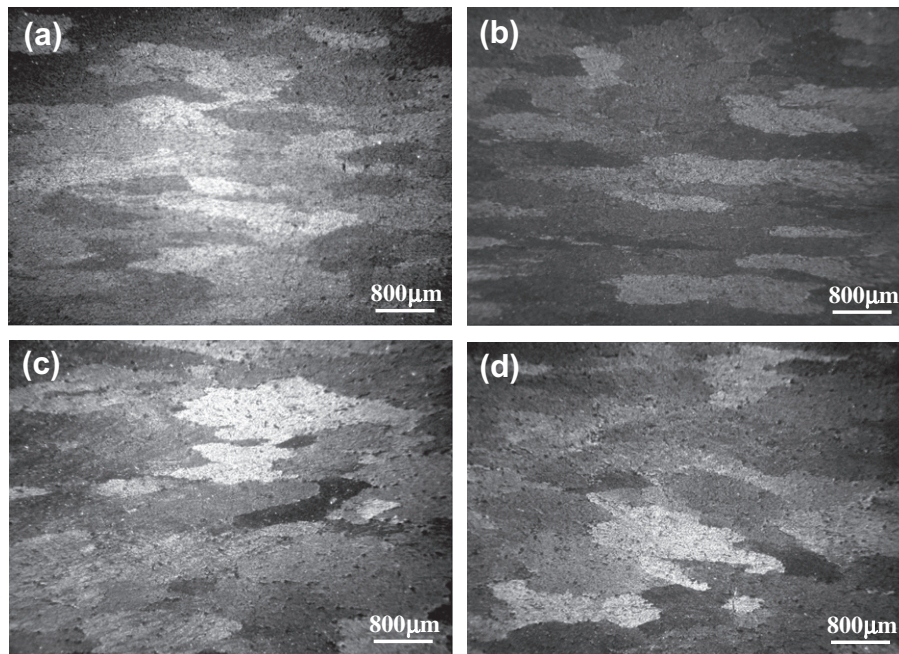
The value of  $\ln(A)$  could then be obtained from the intercept of the  $\ln \dot{\epsilon}$  against  $\ln[\sinh h(\alpha\sigma)]$  plot,  $\ln(A) - Q/RT$ , after the activation energy  $Q$  was calculated using Eq. (3).

The above-mentioned constitutive analysis yielded the values of  $Q$  and the materials parameters in Eq. (1) for the three heat-treated alloys, as given in Table 1. To demonstrate the accuracy of the calculated parameters, the relationship between the measured peak stress ( $\ln[\sinh h(\alpha\sigma)]$ ) and the  $Z$  parameter ( $\ln(Z)$ ) was plotted for each state, as shown in Fig. 6. The lines with slope  $n$  and intercept  $\ln(A)$ , using the calculated constants in Table 1 for each state, were also given in the figure. It is clear that they match pretty well. Regression analysis revealed that for all the cases, the correlation coefficients  $R$  are higher than 0.98, which indicates that the proposed constitutive equations can provide a reliable estimate of the flow stresses.

The activation energies  $Q$  for states 1–3 are 166, 223 and  $172 \text{ kJ mol}^{-1}$ , respectively. State 2 exhibits the highest activation energy, while states 1 and 3 possess similar value with the latter being a bit higher than the former. Change in activation energy with different initial microstructures is well consistent with the change in flow stress. It is highly possible that the difference in the activation energy is the result of the different concentration of Si in the  $\alpha$ -Al solid solution. State 2 was featured by a high dissolved Si content in the matrix, which dramatically increased the work-hardening degree. As a result, deformation became difficult and activation energy increased for state 2.

### 3.4. Microstructures after hot compression

Specimens after hot compression were anodized and examined under polarized light. Microstructure observation revealed a distinct degree of recrystallization under various deformation conditions. The effects of strain rate on the microstructures can be embodied from Fig. 7, which shows the microstructures of state 3 after deformed at  $450^\circ\text{C}$  as an example. When deformed at a lower strain rate of  $0.01 \text{ s}^{-1}$  (Fig. 7a), the grains present a fiber morphology, indicating only recovery occurs. Increase of the strain

**Fig. 7.** Optical anodized microstructures of state 3 after deformed at  $450^\circ\text{C}$  and a strain rate of (a)  $0.01 \text{ s}^{-1}$ ; (b)  $0.1 \text{ s}^{-1}$ ; (c)  $3 \text{ s}^{-1}$ ; (d)  $10 \text{ s}^{-1}$ .

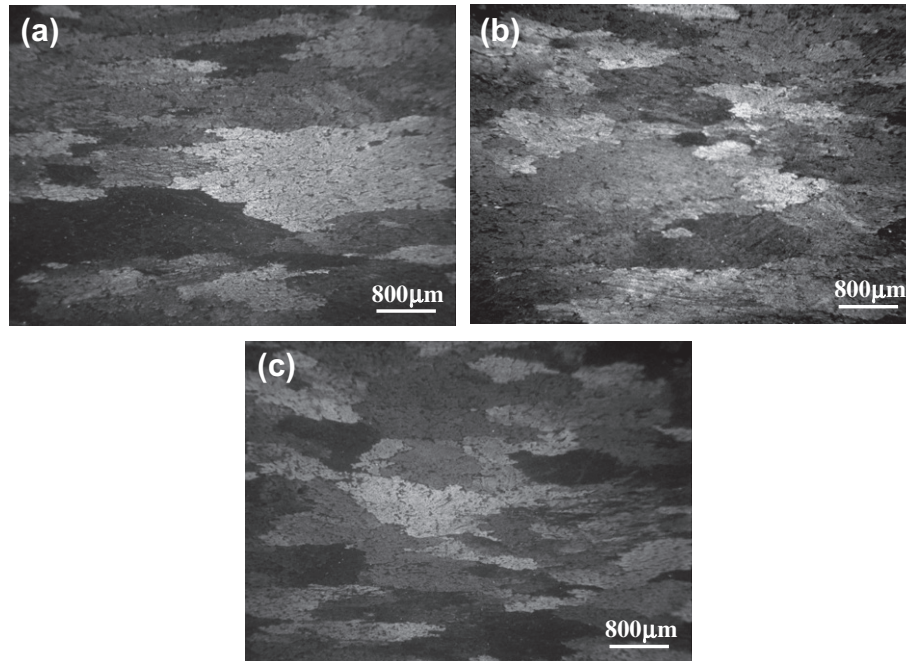


**Fig. 8.** Optical anodized microstructures of state 2 after deformed at (a) 350 °C; (b) 400 °C; (c) 450 °C and a fixed strain rate of  $0.1 \text{ s}^{-1}$ .

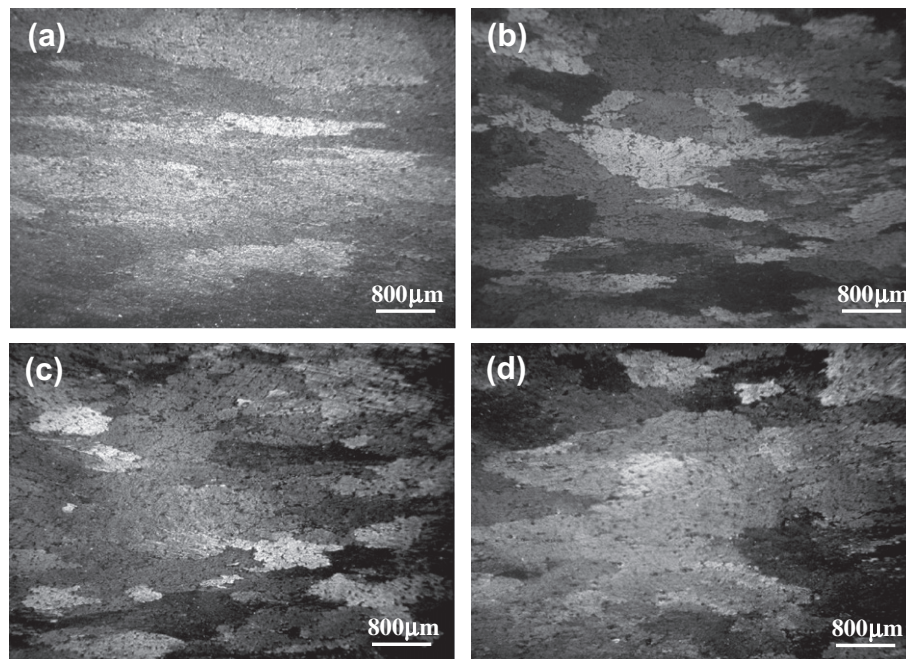


**Fig. 9.** Optical anodized microstructures of state 2 after deformed at 450 °C and a strain rate of (a)  $0.01 \text{ s}^{-1}$ ; (b)  $0.1 \text{ s}^{-1}$ ; (c)  $3 \text{ s}^{-1}$ ; (d)  $10 \text{ s}^{-1}$ .

rate to  $0.1 \text{ s}^{-1}$  (Fig. 7b) and  $3 \text{ s}^{-1}$  (Fig. 7c) leads to a certain degree of recrystallization but elongated deformed grains can still be observed. A full recrystallized homogenous equiaxed grain structure appears when further increasing the strain rate to  $10 \text{ s}^{-1}$  (Fig. 7d). Furthermore, the recrystallization degree increases with temperature at a fixed strain rate, as shown in Fig. 8. It is known that Al alloys possess a high stacking fault [25]; dynamic recovery readily occurs and therefore stored energies during the deformation are timely relieved at lower strain rate. Only when the strain rate increases to a higher level to accumulate enough deformation energies could recrystallization happen. The higher the strain rate, the stronger the driving force, consequently, nuclei rate augments and grains are refined. In addition, atoms diffuse more easily with

the increase of the deformation temperature; the recrystallization degree is thus increased.

Microstructure observation also revealed an obvious effect of different initial states on the deformed microstructures. Fig. 9 gives the deformed microstructures of state 2 at 450 °C and various strain rates. Compared with Fig. 7, the microstructures of state 3 deformed under the same conditions, it is obtained that the minimum strain rate which can stimulate recrystallization shifts to lower value for state 2 compared with state 3. For state 2, an apparent recrystallization takes on at  $0.1 \text{ s}^{-1}$  (Fig. 9b) and complete recrystallization realizes at  $3 \text{ s}^{-1}$  (Fig. 9c); Further increase of the strain rate to  $10 \text{ s}^{-1}$  (Fig. 9d) results in a non-uniform grain structure probably due to heterogeneous grain growth at such a high

deformation temperature. The distinct microstructures strained under  $10\text{ s}^{-1}$  well explain their different flow behaviors, as mentioned before. The deformation activation energy  $Q$  for state 2 is much higher than state 3; sufficient deformation energies could be accumulated at relatively low strain rate. This is why recrystallization occurred at lower strain rate in state 2 than in state 3.

It should be mentioned that state 1 always manifested uneven grain structures after deformation under the experimental conditions. Combined with the microstructure characteristics, this is largely associated with the uneven dispersed precipitates formed during the natural aging. It has been widely accepted that fine particles have strong pinning effects on dislocation motion. Dislocation entanglement and pile-up are therefore more serious at such sites, which are preferred regions for new recrystallized grains to nucleate and grow. The heterogeneous nucleation and unequal subsequent growth speed resulted in a non-uniform grain distribution in the alloy. From this point of view, although it is the least sensitive to the change of the deformation conditions, state 1 should be avoided in industrial practice. Or in other words, the storage period before a homogenized alloy to be hot-worked should be firmly limited, as well as the duration in between the hot-working processes, so as to ensure a more homogenous deformed microstructure.

#### 4. Conclusions

- (1) Based on possible manufacturing practice of 2219 aluminum alloy, three different initial microstructures were designed. Compared to the newly as-homogenized microstructure (state 3), the as-aged state (state 1) was featured by a larger volume fraction of second-phase particles and the as-solutionized microstructure (state 2) was featured by a higher dissolved Si concentration in the  $\alpha$ -Al matrix.
- (2) The activation energies for deformation  $Q$  for states 1–3 were computed to be 166, 223 and  $172\text{ kJ mol}^{-1}$ , respectively. The difference in the activation energy was attributed to the different content of Si in  $\alpha$ -Al solid solution. Under the same deformation conditions, state 2 always showed the highest deformation resistance and state 1 the lowest. Furthermore, state 1 was the least sensitive to the change of the deformation conditions, while state 2 the most.
- (3) The alloy exhibited unstable flow deformation at a high strain rate of  $10\text{ s}^{-1}$ . Especially, while state 3 still underwent a continuous deformation in the whole strain range, both states 1 and 2 showed an abrupt change in the flow curves when strained to approximately 0.6. The abrupt change was considered to be the result of the microstructural change due to the possible precipitation or dissolution occurred during the deformation.
- (4) At a lower strain rate of  $0.01\text{ s}^{-1}$  only dynamic recovery occurred. The recrystallization degree increased with the increase of the strain rate. The minimum strain rate which could stimulate recrystallization shifted to lower value for state 2 compared with state 3. This was due to the higher value of  $Q$  for state 2 in which sufficient deformation energies could be accumulated at relatively low strain rate.
- (5) State 1 always manifested uneven grain structures after deformation under the experimental conditions. It is suggested that in order to ensure a more homogenous deformed microstructure, the storage period before a homogenized alloy to be hot-worked should be firmly limited, as well as the duration in between the hot-working processes.

#### Acknowledgements

The authors are grateful for the financial support of the Natural Science Foundation of CQ CSTC (No. 2008BA4036), sharing fund of Chongqing University's large-scale equipment and Fundamental Research Funds for the Central Universities (CDJXS10131159).

#### References

- [1] Srivatsan TS, Vasudevan S, Park L, Lederich RJ. The quasi-static deformation and final fracture behavior of aluminum alloy 2219. *Mater Sci Eng A* 2008;497:270–7.
- [2] Huang XD, Zhang H, Han Y, Wu WX, Chen JH. Hot deformation behavior of 2026 aluminum alloy during compression at elevated temperature. *Mater Sci Eng A* 2010;527:485–90.
- [3] Pantelakis SG, Alexopoulos ND. Assessment of the ability of conventional and advanced wrought aluminum alloys for mechanical performance in light-weight applications. *Mater Des* 2008;29:80–91.
- [4] Kaibyshev R, Kazakulov I, Gromov D, Musin F, Lesuer DR, Nieh TG. Superplasticity in a 2219 aluminum alloy. *Scr Mater* 2001;44:2411–7.
- [5] Xu WF, Liu JH, Luan GH, Dong CL. Temperature evolution, microstructure and mechanical properties of friction stir welded thick 2219-O aluminum alloy joints. *Mater Des* 2009;30:1886–93.
- [6] Murat T, Ralph TS. Quench sensitivity of 2219–t87 aluminum alloy plate. *Mater Sci Eng A* 2010;527:5033–7.
- [7] Srivatsan TS, Kolar D, Magnussen P. The cyclic fatigue and final fracture behavior of aluminum alloy 2524. *Mater Des* 2002;23:129–39.
- [8] Kaibyshev R, Sitdikov O, Mazurina I, Lesuer DR. Deformation behavior of a 2219 Al alloy. *Mater Sci Eng A* 2002;334:104–13.
- [9] Mazurina I, Sakai T, Miura H, Sitdikov O, Kaibyshev R. Effect of deformation temperature on microstructure evolution in aluminum alloy 2219 during hot ECAP. *Mater Sci Eng A* 2008;486:662–71.
- [10] Rivlin VG, Raynor GV. Phase equilibria in iron ternary alloys – 4. Critical evaluation of constitution of aluminium–iron–silicon system. *Int Met Rev* 1981;26:133–52.
- [11] Mondolfo LF. Aluminium alloys: structure and properties. London: Butterworths; 1976.
- [12] Meredith MW, Worth J, Hamerton RG. Intermetallic phase selection during solidification of Al–Fe–Si(–Mg) alloys. *Mater Sci Forum* 2002;396(402):107–12.
- [13] Allen CM, O'Reilly KAO, Cantor B, Evans PV. Intermetallic phase selection in 1xxx Al alloys. *Prog Mater Sci* 1998;43:89–170.
- [14] Griger A, Stefaniay V, Lendvai A, Turmezey T. Possible modification of cast structure by continuous casting technology in AlFeSi alloys part II: Intermetallic phases. *Aluminium* 1989;65:1049–54.
- [15] Birol Y. Formation and transformation of intermetallic particles in a strip-cast Al–0.8Fe–0.6Si alloy. *Z Metallkde* 1998;89:501–5.
- [16] Zhang J, Pan FS, Zuo RL, Wang WG. Medium temperature phase transformation in AA1235 aluminium sheets for foils. *Chin J Nonferrous Met* 2006;16:1394–9.
- [17] Abouei V, Saghafian H, Shabestari SG, Zarghami M. Effect of Fe-rich intermetallics on the wear behavior of eutectic Al–Si piston alloy (LM13). *Mater Des* 2010;31:3518–24.
- [18] Matsui K. Analysis of factors affecting pinhole formation in rolled aluminium foil. *Kobe Steel Kobe Res Dev* 1990;40:89–92.
- [19] Utsunomiya H, Sutcliffe MPF, Shercliff HR, Bate P, Miller DB. Evolution of matt surface topography in aluminium pack rolling. Part II. Effect of material properties. *Int J Mech Sci* 2004;46:1365–75.
- [20] Zhang J, Pan FS, Zuo RL, Bai CG. The low temperature precipitation in commercial-purity aluminium sheets for foils. *J Mater Process Technol* 2008;206:382–7.
- [21] Sheng ZQ, Shivpuri R. Modeling flow stress of magnesium alloys at elevated temperature. *Mater Sci Eng A* 2006;419:202–8.
- [22] Hu HE, Zhen L, Yang L, Shao WZ, Zhang BY. Deformation behavior and microstructure evolution of 7050 aluminum alloy during high temperature deformation. *Mater Sci Eng A* 2008;488:64–71.
- [23] Yan LM, Shen J, Li JP, Li ZB, Yan XD. Deformation behavior and microstructure of an Al–Zn–Mg–Cu–Zr alloy during hot deformation. *Int J Miner Metall Mater* 2010;17:46–52.
- [24] Lin YC, Chen XM. A critical review of experimental results and constitutive descriptions for metals and alloys in hot working. *Mater Des* 2011;32:1733–59.
- [25] Lawrence EM. Interfacial phenomena in metals and alloys. Boston: Addison-Wesley Publishing Company; 1975.